

15 **Abstract**

16 Most global climate models with convective parameterization have trouble in simulating
17 the observed diurnal cycle of convection. Maximum precipitation usually happens too early
18 during summertime, especially over land. Observational analyses indicate that deep convection
19 over land cannot keep pace with rapid variations in convective available potential energy, which
20 is largely controlled by boundary-layer forcing. In this study, a new convective closure in which
21 shallow and deep convection interact strongly, out of equilibrium, is implemented in atmosphere-
22 only and ocean-atmosphere coupled models. The diurnal cycles of convection in both
23 simulations are significantly improved with small changes to their mean states. The new closure
24 shifts maximum precipitation over land later by about three hours. Compared to satellite
25 observations, the diurnal phase biases are reduced by half. Shallow convection to some extent
26 equilibrates rapid changes in the boundary layer at subdiurnal time scales. Relaxed quasi-
27 equilibrium for convective available potential energy holds in significant measure as a result.
28 Future model improvement will focus on the remaining biases in the diurnal cycle, which may be
29 further reduced by including stochastic entrainment and cold pools.

30 **Key Words:** deep convection; shallow convection; diurnal cycle of precipitation.

31

32 **Plain Language Summary**

33 In this study, we tackled a common challenge in general circulation models concerning
34 the timing of intense rainfall over land during summertime. Many models tend to predict the
35 peak of precipitation too early in the day. To address this, our study introduced a new approach
36 to simulate convection by accounting for the role of shallow convection in stabilizing rapid
37 changes in the atmospheric boundary layer at shorter time scales. This approach delayed
38 maximum precipitation over land by approximately three hours. This adjustment significantly
39 improved the simulated precipitation, aligning them more closely with observations from
40 satellite data. Overall, our research contributes to improving numerical models, bringing them
41 closer to accurately simulating the intricate dynamics of convection and precipitation over land.

42

43 **1 Introduction**

44 Cumulus parameterization is a key component of general circulation models (GCMs). It
45 connects the intensity and vertical structure of sub-grid scale convection with the grid column
46 mean state. Arakawa and Schubert (1974) argued that convection is in quasi-equilibrium, as
47 measured by cloud work function (CWF), closely related to convective available potential
48 energy (CAPE), with forcing due to large-scale processes like advection and radiation. For time
49 scales of order 1 day and beyond, quasi-equilibrium has proved valid based on both theoretical
50 and experimental studies (Jones & Randall, 2011; Neelin & Yu, 1994; Yano & Plant, 2012).
51 However, processes in the planetary boundary layer (PBL) usually exhibit shorter time scales
52 than processes in the free troposphere (Donner & Phillips, 2003; Raymond & Herman, 2011;
53 Zhang, 2002), challenging quasi-equilibrium on these shorter time scales.

54 Convective heat sources, moisture sinks, precipitation, and tracer transports are closely
55 related to convective mass fluxes. The vertical profiles of the mass fluxes are typically
56 determined by using plume models, with the base mass flux determined by a closure. Several
57 convection parameterization schemes following the mass-flux framework have been developed
58 to simulate “equilibrium convection” (Arakawa & Schubert, 1974; Donner et al., 2001; Emanuel,
59 1991; Kain & Fritsch, 1993; Tiedtke, 1989; Zhang & McFarlane, 1995). These schemes show
60 varied abilities in simulating tropical waves and intraseasonal variability (Kim et al., 2011; Lin et
61 al., 2006). The quasi-equilibrium assumption used in the European Centre for Medium-Range
62 Weather Forecasts (ECMWF) Integrated Forecasting System (IFS) is found to reproduce
63 reasonably well the observed mid-latitude synoptic variability, tropical wave spectra and
64 intraseasonal variability (Bechtold et al., 2008; Hirons et al., 2013).

65 In contrast to equilibrium convection, non-equilibrium convection often holds at time
66 scales of several hours (Davies et al., 2013; Jones & Randall, 2011; Yano & Plant, 2012). Non-
67 equilibrium convection usually occurs in the presence of strong free troposphere forcing or
68 surface heat fluxes. During summertime, surface heat fluxes over land are largely modulated by
69 solar insolation. Variations in surface heat fluxes drive rapid changes in CAPE with which
70 convection is out of equilibrium, as is the related strong diurnal cycle of precipitation over land.
71 Overall, the diurnal cycle of convection over land is characterized by shallow convection in the
72 morning with precipitation associated with deep convection peaking in the late afternoon to early
73 evening (Dai et al., 1999; Tian et al., 2005). It is challenging for state-of-art GCMs to correctly

74 simulate the observed diurnal cycle of precipitation over land. Model-simulated maximum
75 precipitation over land usually happens too early and its phase closely follows the phase of
76 surface fluxes that are largely determined by solar radiation (Dong et al., 2023a; Stratton &
77 Stirling, 2012; Zhao et al., 2018b). While coarse-resolution GCMs struggle in simulating the
78 observed diurnal cycle of convection, the observed diurnal cycle can be simulated reasonably in
79 cloud resolving models with resolutions of order 2.5 km or higher (Petch et al., 2002; Stirling &
80 Stratton, 2012). This study addresses convective parameterization in coarse-resolution GCMs.

81 Apart from resolution, previous studies have explored various strategies to improve the
82 diurnal cycle of convection, including but not limited to entrainment rates (Del Genio & Wu,
83 2010; Piriou et al., 2007; Stratton & Stirling, 2012), a prognostic closure accounting for
84 convective memory (Gerard et al., 2009; Pan & Randall, 1998), convective closures including
85 convective inhibition and cold pools (Fletcher & Bretherton, 2010; Mapes, 2000; Rio et al.,
86 2009), a convective triggering function (Xie et al., 2019), and humidity (Fuchs & Raymond,
87 2007). However, these approaches have not proved to be universally suited for GCMs. An
88 alternate strategy is suggested by observational analyses showing that CAPE variability is
89 controlled by boundary-layer variability, emphasized by Donner and Phillips (2003) and
90 consistent with analyses by Zhang (2002, 2003). In light of this, Bechtold et al. (2014) proposed
91 augmenting the relaxed quasi-equilibrium closure often used for deep convection by a non-
92 equilibrium term accounting for the inability of deep convection to equilibrate CAPE changes
93 resulting from rapid non-convective PBL processes. Improvements in the ECMWF IFS diurnal
94 cycle using this closure encouraged us to explore non-equilibrium convection in the Geophysical
95 Fluid Dynamics Laboratory (GFDL) climate models.

96 In this study, we show that including non-equilibrium, shallow convection in the closure
97 for deep convection significantly improves the simulation of the diurnal cycle in GFDL AM4
98 (atmosphere) (Zhao et al., 2018a, 2018b) and CM4 (coupled ocean-atmosphere) (Held et al.,
99 2019) models, while still leaving a notable bias. Section 2 describes the non-equilibrium closure
100 for deep convection. Section 3 shows that changing the deep convection closure in AM4 and
101 CM4 improves diurnal precipitation cycles while changing only slightly other key simulation
102 characteristics. In Section 4 we summarize and suggest possible further ways to improve
103 simulation of the diurnal cycle of convection. In the Appendix, we relate this closure based on
104 relaxed quasi-equilibrium including both deep and shallow (non-equilibrium) convection to a

105 non-equilibrium closure in which CAPE changes are controlled by non-convective PBL
 106 processes. We show that shallow convection responds strongly to changes produced by rapid
 107 non-convective PBL processes. In the limit where shallow convection equilibrates non-
 108 convective PBL processes, the two non-equilibrium closures are identical.

109 2 Method and Experiments

110 2.1 Non-Equilibrium Convection

111 An established method for parameterizing convection is balancing CAPE or CWF
 112 changes produced by deep convection with a relaxation of CAPE or CWF changes by non-
 113 convective processes, notably large-scale advection, surface fluxes, radiative cooling, and eddy
 114 diffusion (Moorthi & Suarez, 1992; Zhang & McFarlane, 1995). Several generations of GFDL
 115 climate models have adopted this approach (Anderson et al., 2004; Donner et al., 2011; Zhao et
 116 al., 2018a), and all have suffered from large biases in their diurnal cycles of precipitation, mostly
 117 over land but also to a lesser degree over ocean. Based on observational analysis showing this
 118 balance does not hold at sub-diurnal time scales (Donner & Phillips, 2003; Zhang, 2002, 2003),
 119 we generalize this balance to include non-equilibrium convection. The processes changing CAPE
 120 are:

$$121 \quad \left(\frac{\partial \text{CAPE}}{\partial t}\right) = \left(\frac{\partial \text{CAPE}}{\partial t}\right)_{\text{nc,BL}} + \left(\frac{\partial \text{CAPE}}{\partial t}\right)_{\text{nc,FT}} + \left(\frac{\partial \text{CAPE}}{\partial t}\right)_{\text{deep}} + \left(\frac{\partial \text{CAPE}}{\partial t}\right)_{\text{shal}} \quad (1)$$

122 Here, the subscript “nc” refers to all non-convective processes. “BL” refers to changes in the
 123 PBL, while changes in the overlying free troposphere are denoted by “FT”. These tendencies are
 124 easily computed in a model using tendencies from the dynamical core and parameterizations for
 125 radiative transfer, surface fluxes, and sub-grid diffusion. The subscripts “deep” and “shal” refer
 126 to CAPE changes from deep and shallow convection, respectively.

127 Quasi-equilibrium (Arakawa & Schubert, 1974) has been proposed as a closure for
 128 convective mass fluxes, to which are related convective heat sources, moisture sinks,
 129 precipitation, and tracer transport. Quasi-equilibrium posits:

$$130 \quad \left(\frac{\partial \text{CAPE}}{\partial t}\right) \ll \left(\frac{\partial \text{CAPE}}{\partial t}\right)_{\text{nc,BL}} + \left(\frac{\partial \text{CAPE}}{\partial t}\right)_{\text{nc,FT}} \quad (2)$$

131 When (2) holds, convective CAPE tendencies balance non-convective CAPE tendencies. The
 132 convective mass fluxes are then obtained from the convective CAPE tendencies. Observations

133 show that quasi-equilibrium is a reasonable approximation as diurnal time scales are approached
 134 but does not hold for sub-diurnal time scales (Donner and Phillips, 2003, Fig. 2). A recourse is to
 135 relax the non-convective terms in (1):

$$136 \quad \left(\frac{\partial \text{CAPE}}{\partial t}\right)_{\text{nc,BL}} + \left(\frac{\partial \text{CAPE}}{\partial t}\right)_{\text{nc,FT}} = \frac{\text{CAPE} - \text{CAPE}_0}{\tau} \quad (3)$$

137 In Eq. (3), CAPE_0 is a reference value toward which CAPE, having evolved by non-
 138 convective processes since its last adjustment due to convection (the beginning of a model time
 139 step in AM4), relaxes over an extended time τ . The value of τ is typically tuned to multiple
 140 hours in models. Based on field experiments, Donner and Phillips (2003) estimated CAPE_0 to be
 141 0 J kg^{-1} , and τ to be 6.5 hours. Zhao et al. (2018b) tuned these to 10 J kg^{-1} and 8 hours,
 142 respectively, in AM4.

143 The relaxed CAPE tendency is then assumed to be in quasi-equilibrium with convective
 144 tendencies, implying:

$$145 \quad \left(\frac{\partial \text{CAPE}}{\partial t}\right)_{\text{deep}} = -\frac{\text{CAPE} - \text{CAPE}_0}{\tau} - \left(\frac{\partial \text{CAPE}}{\partial t}\right)_{\text{shal}} \quad (4)$$

146 In GFDL AM2, AM3, and AM4, the contribution from non-equilibrium shallow
 147 convection has not been included in the determination of the deep convective CAPE tendency
 148 and mass fluxes. Rather, only deep convection has been assumed to be in relaxed equilibrium
 149 with non-convective tendencies. Shallow convective tendencies are likely to be non-equilibrium
 150 and tied closely to the evolution of the PBL. In GFDL AM3 and AM4, shallow convective base
 151 mass fluxes M_{shal} follow Bretherton et al. (2004):

$$152 \quad M_{\text{shal}} \propto \sqrt{c_1 \text{TKE}} \exp\left(-\frac{c_2 \text{CIN}}{\text{TKE}}\right) \quad (5)$$

153 where TKE denotes PBL turbulent kinetic energy; CIN, convective inhibition; and c_1 and c_2
 154 denote constants. $\left(\frac{\partial \text{CAPE}}{\partial t}\right)_{\text{shal}}$ in Eq. (4) depends strongly on M_{shal} . We hypothesize that non-
 155 equilibrium shallow convection and its diurnal cycle are important in the relaxed balance in Eq.
 156 (4). By removing enthalpy and moisture from the boundary layer, shallow convection generally
 157 reduces CAPE (Figs. A1a,b and A2a,b), though infrequent exceptions of small magnitude can
 158 occur, for example, for a PBL cold and dry relative to the free troposphere above.

159 **2.2 Observations and Implementation in AM4 and CM4**

160 For observations, we use the NASA Global Precipitation Measurement (GPM) Integrated
161 Multisatellite Retrievals for GPM (IMERG) (Huffman et al., 2015) to evaluate the models'
162 ability in simulating the diurnal cycle of precipitation. IMERG provides a global-gridded product
163 with 0.1° horizontal resolution and 30-min frequency. For a direct comparison with AM4 and
164 CM4 outputs, the IMERG product is re-gridded to 1.0° latitude \times 1.25° longitude resolution. In
165 addition, Global Precipitation Climatology Project (GPCP v3.2)(Huffman et al., 2022) is used to
166 evaluate the mean precipitation climatology. The high-frequency IMERG observations are well-
167 suited for evaluating the diurnal cycle, while the combination of surface and satellite
168 observations in GPCP are better suited for evaluation of long-term means. Radiation at the top of
169 the atmosphere from CERES EBAF Edition 4.1 (Loeb et al., 2018) is used to evaluate the
170 models' energy budget. Monthly ERA5 data (Hersbach et al., 2020) is used for temperature
171 comparisons .

172 AM4 with prescribed sea surface temperatures (SSTs) and sea ice, and pre-industrial (PI)
173 CM4 ocean-atmosphere coupled model are used to explore the effects of non-equilibrium
174 convection. Detailed descriptions of AM4 can be found in Zhao et al. (2018a, 2018b), and CM4
175 is documented in Held et al. (2019). In both AM4 and CM4, the atmosphere component has 33
176 vertical levels with a horizontal resolution of approximately 100 km. The PI configuration of
177 CM4 is chosen because the PI period is in global energy balance (unlike present day), rendering
178 an evaluation of PI model drift and energy cycle more straightforward than for an evolving
179 historical simulation, which would, in any case, need to start from a realistic, balanced PI
180 simulation.

181 We implement a non-equilibrium closure based on Eq. (4) including the CAPE tendency
182 due to shallow convection and examine its impact on the diurnal cycle of precipitation in AM4
183 and CM4 in subsequent sections. Default configurations of the standard AM4 documented in
184 Zhao et al. (2018a, 2018b) used a relaxed quasi-equilibrium closure where CWF changes
185 induced by deep convection are balanced by a relaxation of CWF changes due to non-convective
186 processes. Here, we implement relaxed quasi-equilibrium using CAPE instead of CWF (Eqs. (3)
187 and (4)). Doing so facilitates computations of changes with respect to state changes, which are
188 easily done for CAPE but require additional convective plume calculations for CWF. In this
189 study, the CWF based quasi-equilibrium closure is referred to as standard AM4. The CAPE

190 based non-equilibrium closure based on Eq. (4) including the CAPE tendency due to shallow
 191 convection is referred to as relax QE D+S. Two parameters are retuned in relax QE D+S from
 192 those in standard AM4. The retuning simulates Earth's energy imbalance in the relax QE D+S
 193 AMIP integration (2001-2014) to a value of 1.08 W/m^2 , close to CERES EBAF (0.88 W/m^2).
 194 The retuned parameters (1) increase ice fall speeds by 10% and (2) change cloud-top entrainment
 195 in stratiform clouds to increase absorbed shortwave radiation (SWABS) at top of the atmosphere
 196 (TOA). For CM4, the PI-Control simulation uses the quasi-equilibrium closure based on CWF.
 197 The PI simulation using the CAPE based non-equilibrium closure based on Eq. (4), with the
 198 same two retuned parameters, is referred to as PI relax QE D+S. Table 1 lists the experiments
 199 and observational products.

200 Bechtold et al. (2014) provide an alternate interpretation for non-equilibrium convection.
 201 Its incorporation in the ECMWF IFS improved its diurnal precipitation cycle. The Appendix
 202 shows the approach here, when implemented in AM4, is closely related.

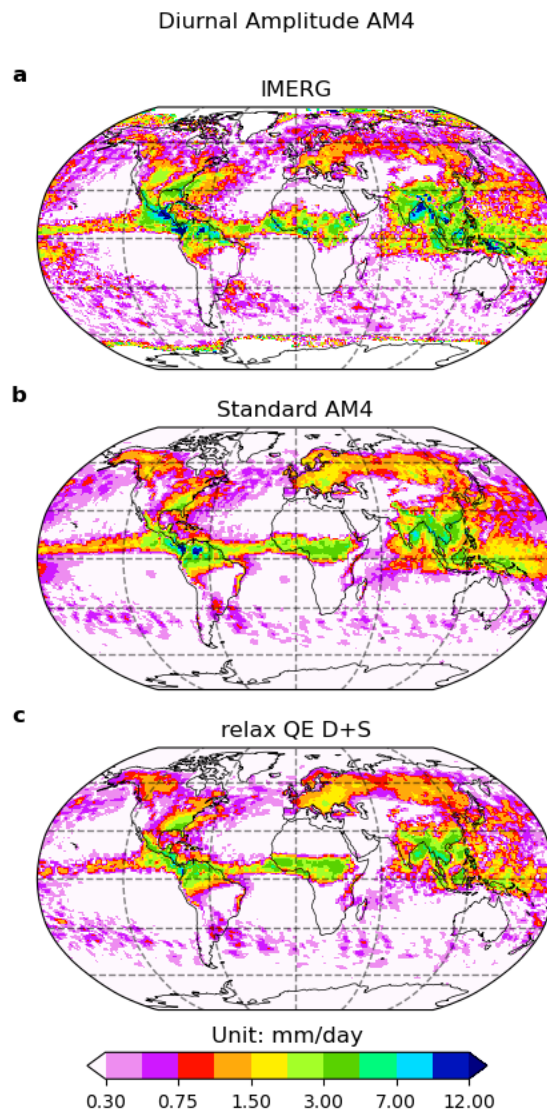
203

204 Table 1 Experiments and observations.

Data Source	Experiment Name	Resolution	Time
AM4	Standard AM4	1.0° lat x 1.25° lon	Prescribed SSTs (Rayner et al., 2003) from 1979-2014
	relax QE D+S		
CM4	PI-Control		200 years
	PI relax QE D+S		
Observation	IMERG	0.1° original and re-gridded to 1.0° lat, 1.25° lon	2001-2014
	GPCP v3.2	2.5° lat x 2.5° lon	2001-2014
	CERES EBAF Edition 4.1	1.0° lat x 1.0° lon	2001-2014
	ERA5	0.25° lat x 0.25° lon	2001-2014

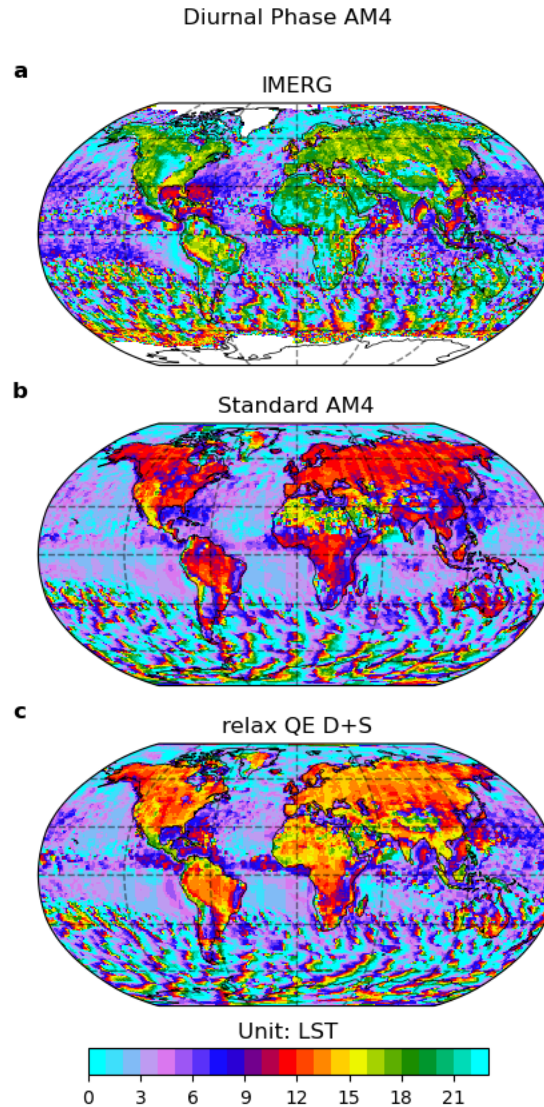
205 **3. Results**206 **3.1 Diurnal Precipitation Cycle in AM4**

207 To quantify the diurnal amplitude and phase of precipitation, the model outputs and
208 satellite observations are first composited in hourly bins. A Fourier analysis is then applied to the
209 hourly-binned data to get its first harmonic. Figure 1 compares the diurnal amplitude of boreal
210 summer precipitation between IMERG, standard AM4 and relax QE D+S. The observed spatial
211 distribution of diurnal amplitude shows notable peaks over central America, northern Amazon,
212 central Africa, south Asia, and Maritime Continent. Overall, the pattern of the diurnal amplitude
213 is similar for standard AM4 and relax QE D+S, indicating that the modified closure has little
214 impact on the diurnal amplitude of precipitation.



215

216 Figure 1 Diurnal amplitude of precipitation (unit: mm day^{-1}) during boreal summer (June-
 217 August) for (a) IMERG, (b) Standard AM4, and (c) relax QE D+S.



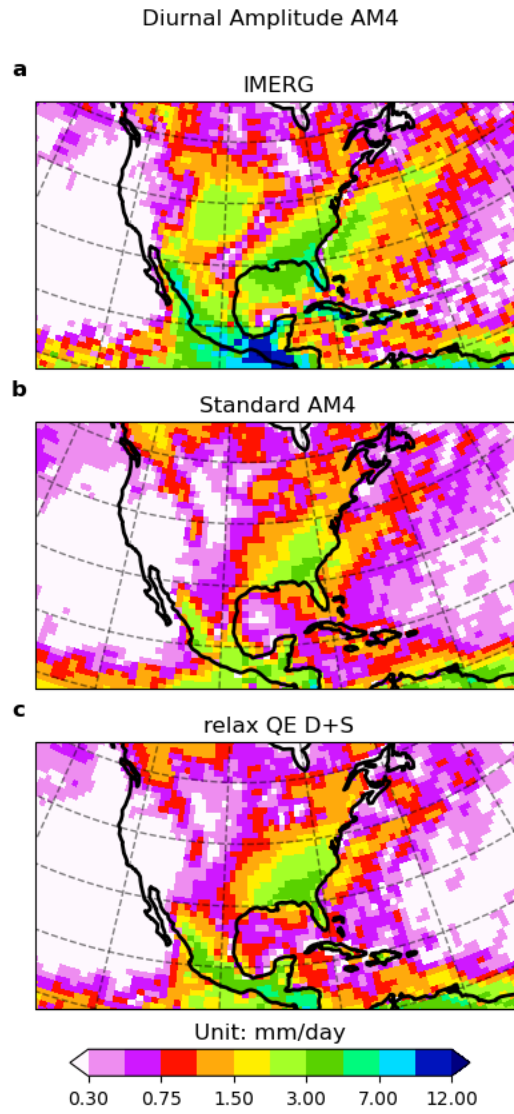
218
 219 Figure 2 Diurnal phase (unit: LST hour) during boreal summer (June-August) for (a) IMERG,
 220 (b) Standard AM4, and (c) relax QE D+S.

221 The diurnal phase (local solar time, LST) is shown in Figure 2. For IMERG, maximum
 222 precipitation over land occurs mostly from late afternoon to early evening. Over tropical oceans,
 223 maximum precipitation predominantly occurs in early morning, although certain regions, such as
 224 the Gulf of Mexico and coastal regions off central America and south Asia, exhibit peak
 225 precipitation in late morning to local noon (Figure 2a). The largest phase errors in standard AM4
 226 are generally over land. Maximum precipitation over land in standard AM4 occurs around local
 227 noon (Figure 2b), which is too early compared to IMERG and is a known issue in AM4 (Zhao et

228 al., 2018a). In relax QE D+S, the diurnal cycle over land is delayed by about three hours relative
229 to standard AM4 (Figure 2c), which means the phase biases between standard AM4 and IMERG
230 are reduced by half. The significant improvement indicates that shallow convection strongly
231 mediates rapid variations in CAPE at subdiurnal time scales consistent with observational
232 analyses shown in Donner and Phillips (2003). The retuning of relax QE D+S discussed in
233 Section 2 does not change Figure 2 noticeably (not shown).

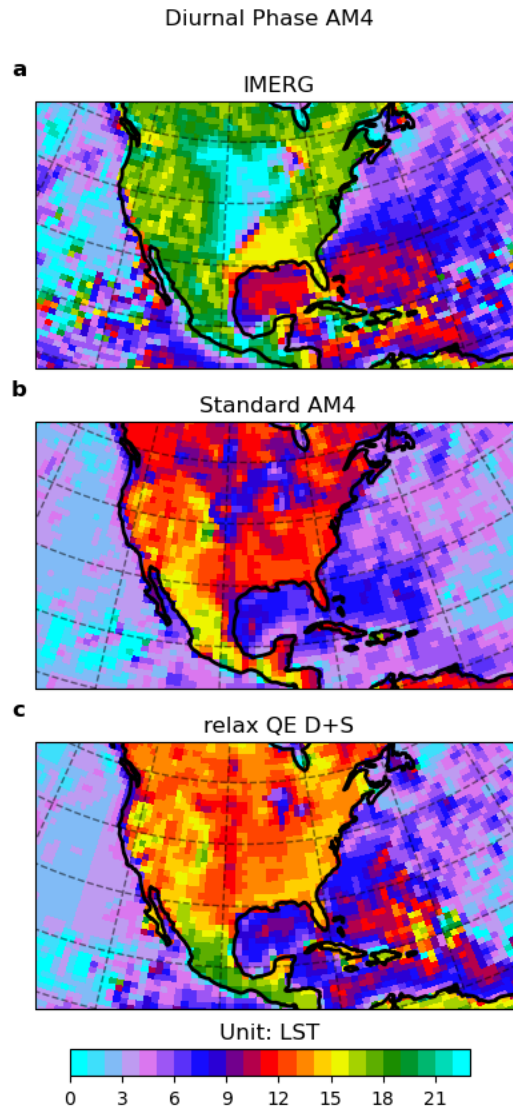
234 Next, we focus on the diurnal cycle over the contiguous United States during boreal
235 summer (CONUS; Figure 3). The observed diurnal amplitude shows peaks eastward of the
236 Rocky Mountains area and over the southeast CONUS and the corresponding coastal regions
237 (Figure 3a). Standard AM4 reasonably reproduces the diurnal amplitude over the southeast
238 CONUS but underestimates the diurnal amplitude east of the Rocky Mountains (Figure 3b).
239 Compared to standard AM4, relax QE D+S shows a similar spatial pattern of the diurnal
240 amplitude (Figure 3c), which again indicates that the revised closure has little impact on the
241 spatial pattern of the diurnal amplitude.

242



243

244 Figure 3 Same as Figure 1 but over the contiguous United States.



245

246 Figure 4 Same as Figure 2 but over the contiguous United States.

247

248

249

250

251

252

253

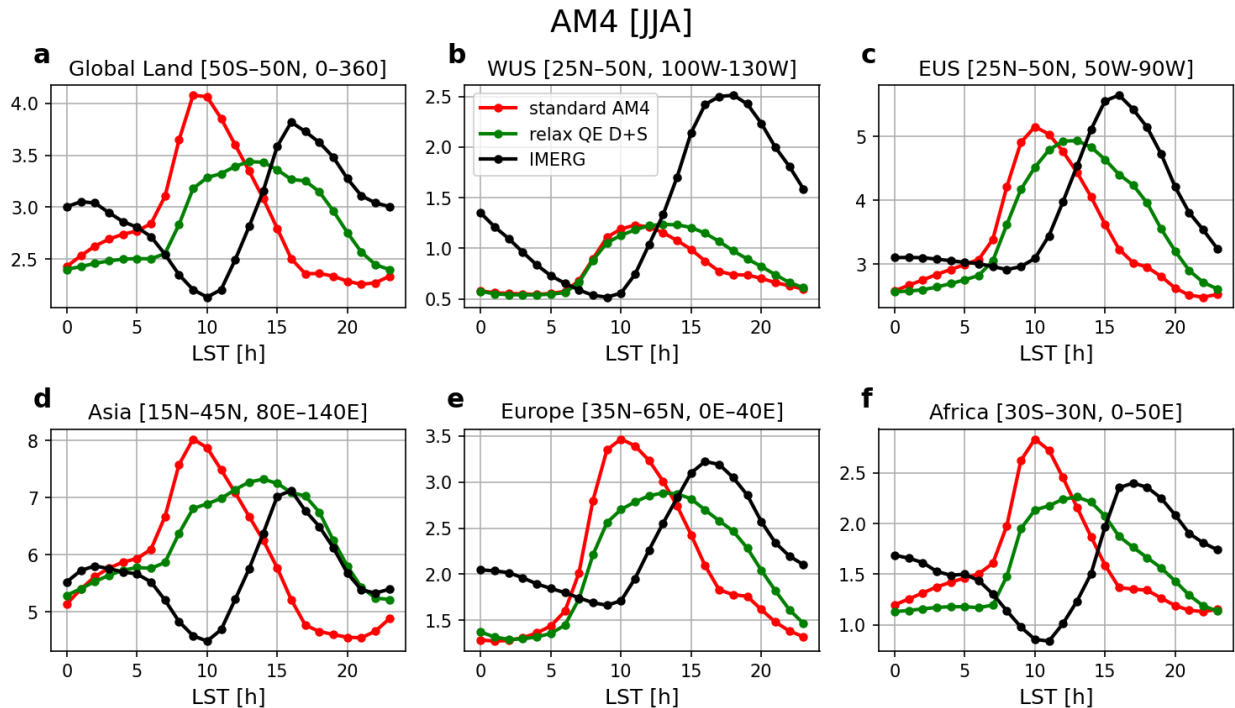
254

255

For the diurnal phase, the observed spatial pattern in IMERG is characterized predominantly by late afternoon convection over the western and eastern United States, and nighttime convection over Central Plains due to mesoscale convective systems (Figure 4a), which is consistent with previous results (Bechtold et al., 2014; Dai et al., 1999; Dong et al., 2023b; Tian et al., 2005; Watters et al., 2021). The diurnal phase in standard AM4 is significantly biased from IMERG with maximum precipitation occurring around local noon in most parts of CONUS (Figure 4b). By including the modulation of CAPE by shallow convection in the closure for deep convection, relax QE D+S shifts the diurnal cycle later by about three hours. The diurnal phase is also improved over the surrounding ocean, especially the Gulf of

256 Mexico and coastal regions off the southeast CONUS (Figure 4c). Bechtold et al. (2014) showed
257 similar improvement of the diurnal cycle, globally and over CONUS, with non-equilibrium
258 convection implemented in the ECMWF IFS (their Figures 2 and 4), also with small changes in
259 CONUS amplitudes (their Figure 3). This suggests the closure based on Eq. (4) may be related to
260 the non-equilibrium closure implemented in Bechtold et al. (2014). The Appendix discusses this
261 in detail.

262 The improved diurnal cycle is further confirmed by domain-averaged precipitation
263 without projection onto a single harmonic. The overall improvement over land areas holds
264 globally (Figure 5a) and at regional scales (Figure 5b-f). Compared to standard AM4, relax QE
265 D+S weakens convective activity around local noon time but enhances it during late afternoon
266 and early evening. The extent to which the diurnal cycle improves varies with location. For
267 example, the diurnal cycle over the western United States shows less improvement than over the
268 eastern United States. One possible reason is that AM4 with coarse horizontal resolutions is not
269 able to simulate well mesoscale connective systems east of the Rocky Mountains indicated by
270 Figure 3. The improved diurnal cycles over Asia, Europe, and Africa are consistent and
271 comparable to those reported by Bechtold et al. (2014) (their Figure 5). Although the diurnal
272 cycle of convection in relax QE D+S is significantly improved compared to the observations, the
273 late-night precipitation in relax QE D+S is still underestimated. As mentioned by Bechtold et al.
274 (2014), the late-night precipitation deficit may relate to the missing representation of surface cold
275 pools and upper-level mesoscale lifting.



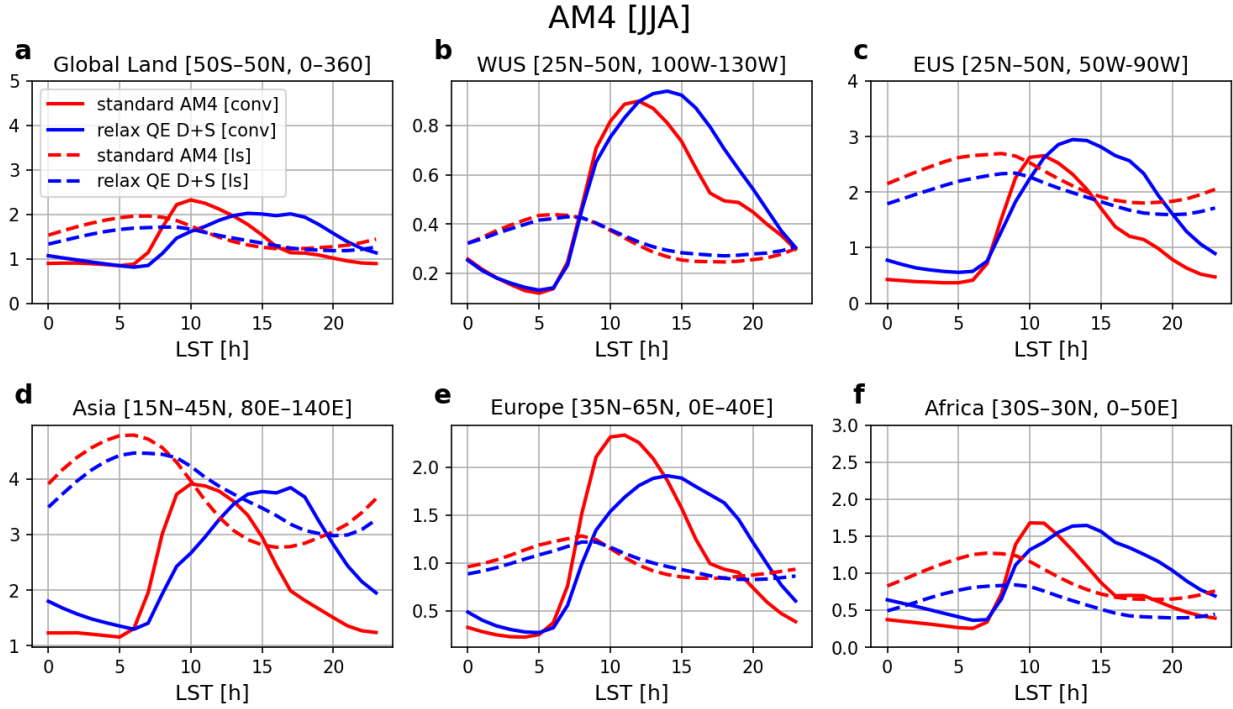
276

277 Figure 5 Domain averaged hourly land precipitation (units: mm day⁻¹) averaged from June to
 278 August for Standard AM4 (red lines), relax QE D+S (green lines), and IMERG (black lines) over
 279 (a) Global Land, (b) Western United States, (c) Eastern United States, (d) Asia, (e) Europe, and
 280 (f) Africa.

281 The total precipitation in AM4 consists of contributions from convective and large-scale
 282 parameterizations. We decompose the total precipitation into the convective and large-scale
 283 components (Figure 6). Overall, the convective precipitation peaks a few hours later in relax QE
 284 D+S than in standard AM4. The large-scale component is only slightly affected by relax QE
 285 D+S. The improved diurnal cycle of total precipitation shown in Figure 5 is mostly contributed
 286 by a better representation of the convective precipitation.

287 The phase changes in Figures 1-5 are strongly dominated by including the $\left(\frac{\partial \text{CAPE}}{\partial t}\right)_{shal}$
 288 term in Eq. (4). There are only small contributions to the phase changes from using relaxed
 289 CAPE instead of relaxed CWF in Eqs. (3) and (4) and from tuning for relax QE D+S.

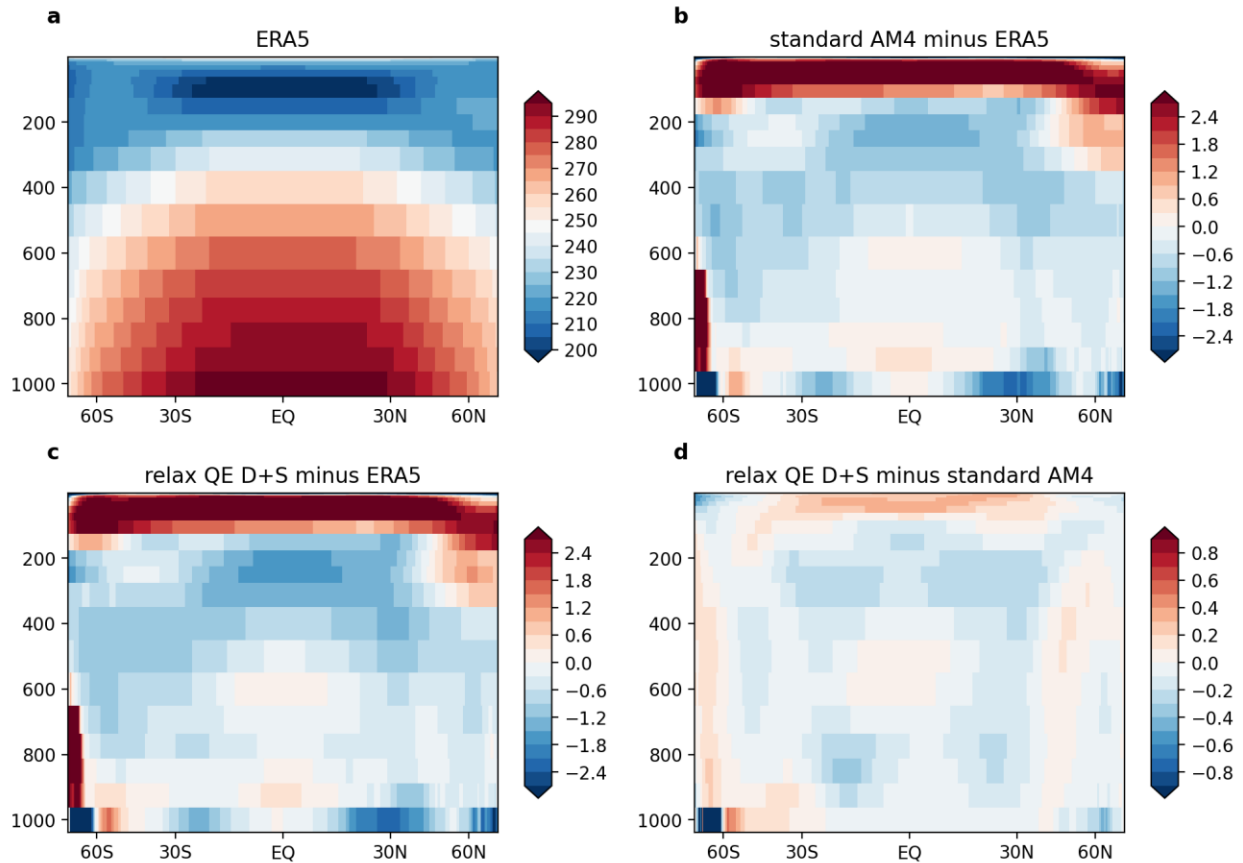
290



291
 292 Figure 6 As in Figure 5 except showing a decomposition of the total precipitation into
 293 parameterized convection (solid lines) and large scale (dash lines) over the same regions.

294 **3.2 Mean State and Tropical Variability in AM4**

295 Figure 7 compares zonal mean temperature between ERA5, standard AM4 and relax QE
 296 D+S. Overall, both standard AM4 and relax QE D+S show colder troposphere but warmer
 297 stratosphere than ERA5 (Figure 7b and Figure 7c). In the tropics, standard AM4 is mostly
 298 warmer in the troposphere but colder in the stratosphere than relax QE D+S (Figure 7d).
 299 Temperature changes from replacing CWF in Standard AM4 with CAPE in the relaxation terms
 300 in Eqs. (3) and (4) are similar in pattern, larger in magnitude, but opposite in sign to those in
 301 Figure 7d. Temperature changes associated with the $\left(\frac{\partial CAPE}{\partial t}\right)_{shal}$ term in Eq. (4) largely oppose
 302 those from replacing CWF with CAPE in the relaxation, as do tuning changes to obtain relax QE
 303 D+S. (These intermediate changes are not shown.)



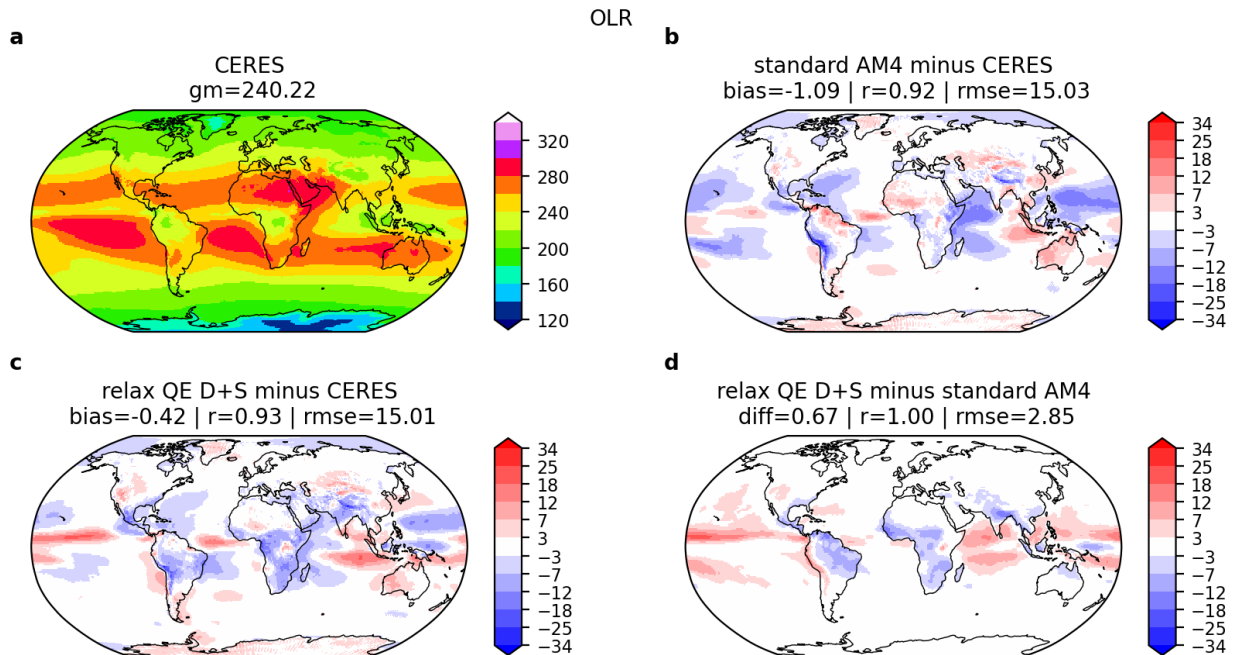
304
305

306 Figure 7 2001-2014 annual, zonal mean air temperature (units: K) for (a) ERA5, (b) standard
307 AM4 minus ERA5, (c) relax QE D+S minus ERA5, and (d) relax QE D+S minus standard AM4.

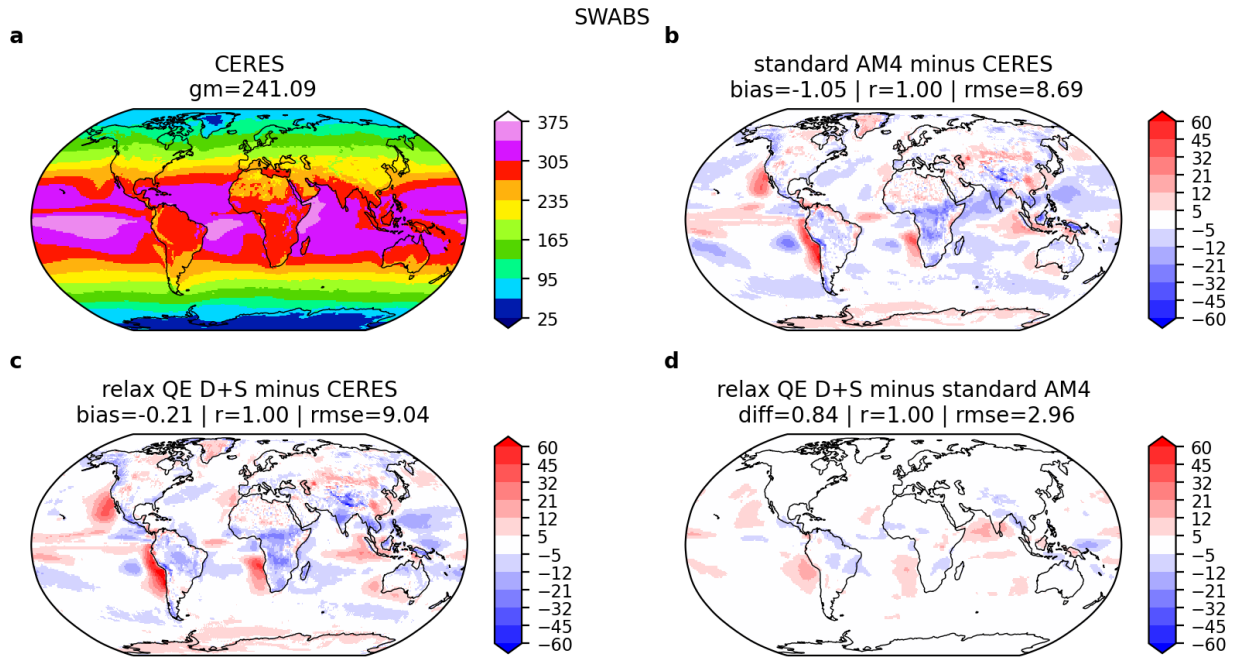
308 Outgoing longwave radiation (OLR) in standard AM4 and relax QE D+S are overall
309 similar to CERES-EBAF observations with some regional differences (Figure 8). Compared to
310 standard AM4, relax QE D+S shows enhanced OLR over tropical ocean but reduced OLR over
311 land, although the global mean OLR in relax QE D+S is slightly greater than that in standard
312 AM4 (Figure 8d). The absorbed shortwave radiation (SWABS) patterns are also similar between
313 standard AM4 and relax QE D+S but relax QE D+S also has slightly greater global mean
314 SWABS than standard AM4 (Figure 9). As a result, the energy imbalance at TOA does not
315 change much between standard AM4 and relaxed QE D+S. In addition, standard AM4 and relax
316 QE D+S show similar spatial patterns of mean precipitation, with global mean precipitation in
317 both experiments greater than GPCP (Figure 10). The precipitation intensity distribution is
318 almost identical between standard AM4 and relax QE D+S in the tropics, northern hemisphere
319 mid-latitudes, and southern hemisphere mid-latitudes (Figure 11). The precipitation intensity
320 distribution also remains nearly unchanged between standard AM4 and relax QE D+S when land

321 and ocean are considered separately (not shown), indicating that the new non-equilibrium closure
 322 does not affect the overall precipitation statistics. Moreover, the tropical wave spectra analyses
 323 show only small changes between standard AM4 and relax QE D+S (Figure 12).

324 We also conducted idealized experiments with uniform SST warming by 2K to examine
 325 the ‘Cess sensitivity’ (Cess et al., 1990), which is computed by examining the change in net
 326 TOA flux in response to uniform 2K ocean warming. We found that relax QE D+S yields a Cess
 327 sensitivity of 0.54-0.55 K W⁻¹ m², which is very similar to the value (0.56-0.57 K W⁻¹ m²)
 328 reported by Zhao et al. (2018a), indicating that the implementation of the revised closure has
 329 little impact on the model’s global mean radiative response to uniform SST warming.



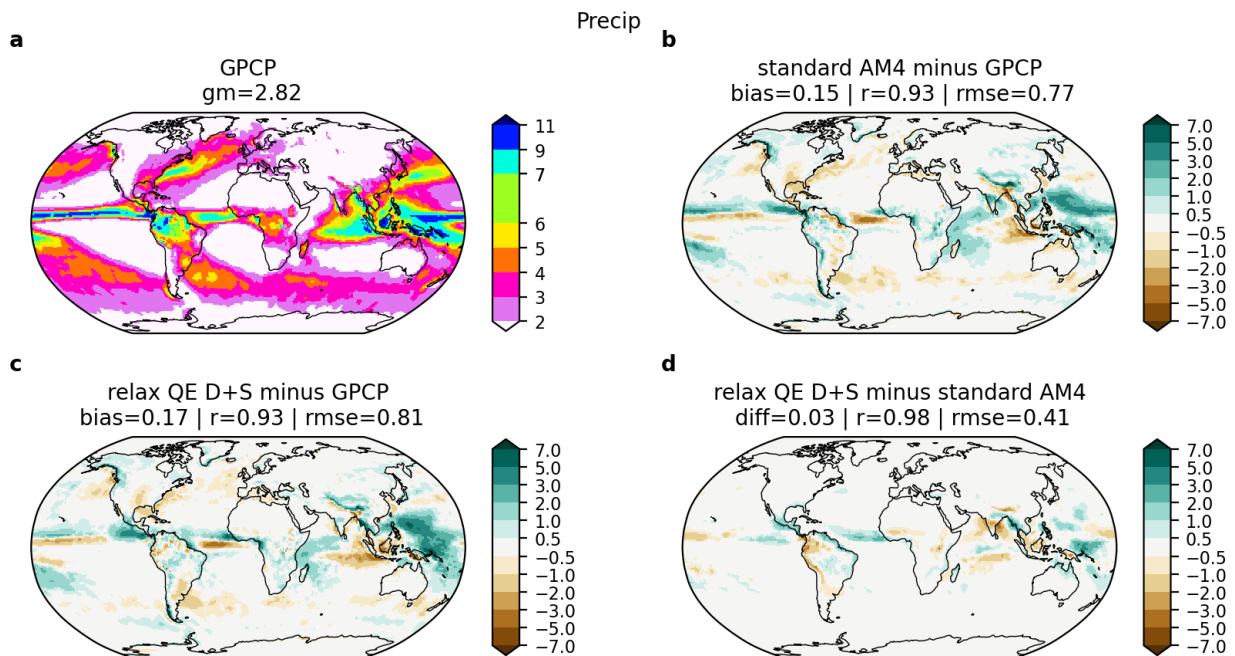
330
 331 Figure 8 2001-2014 annual mean OLR (units: W m⁻²) for (a) CERES EBAF, (b) standard AM4
 332 minus CERES EBAF, (c) relax QE D+S minus CERES EBAF, and (d) relax QE D+S minus
 333 standard AM4. Bias (or difference), correlation coefficient, and root mean square error are listed.



334

335 Figure 9 Same as Figure 8 but for SW radiation at TOA (units: $W m^{-2}$).

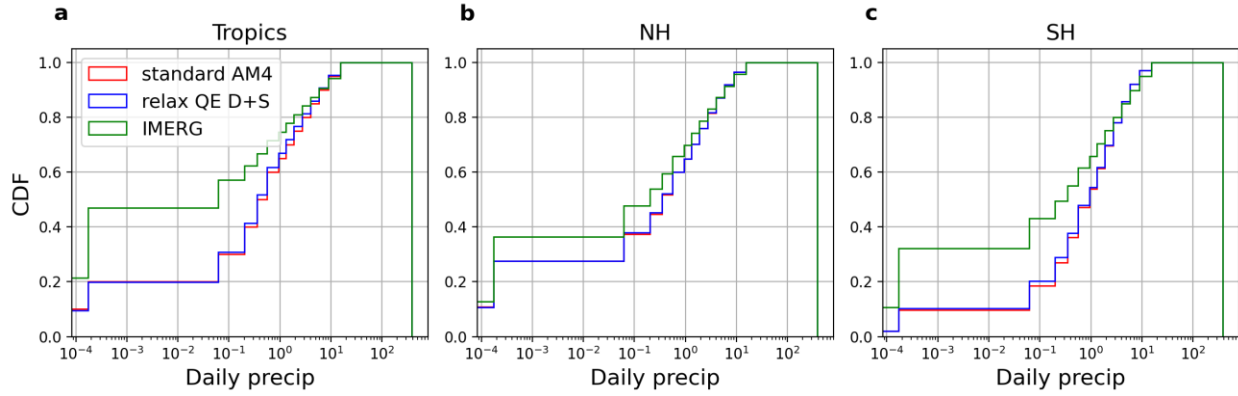
336



337

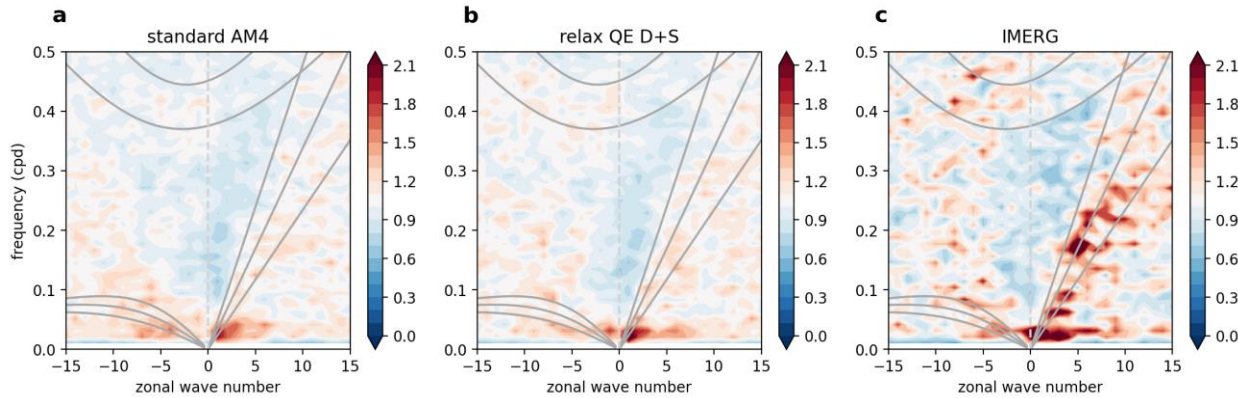
338 Figure 10 2001-2014 annual mean precipitation (units: $mm day^{-1}$) for (a) GPCP, (b) relax QE
339 D+S minus GPCP, (c) relax QE D+S minus GPCP, and (d) relax QE D+S minus standard AM4.
340 Bias (or difference), correlation coefficient, and root mean square error are listed.

341



342
 343 Figure 11 Cumulative distribution of precipitation over (a) Tropics (30°S-30°N), (b) Northern
 344 Hemisphere Mid-latitude (30°N-60°N), and (c) Southern Hemisphere Mid-latitude (60°S-30°S).
 345 Red curves for standard AM4, Blue for relax QE D+S, and Green for IMERG.

346

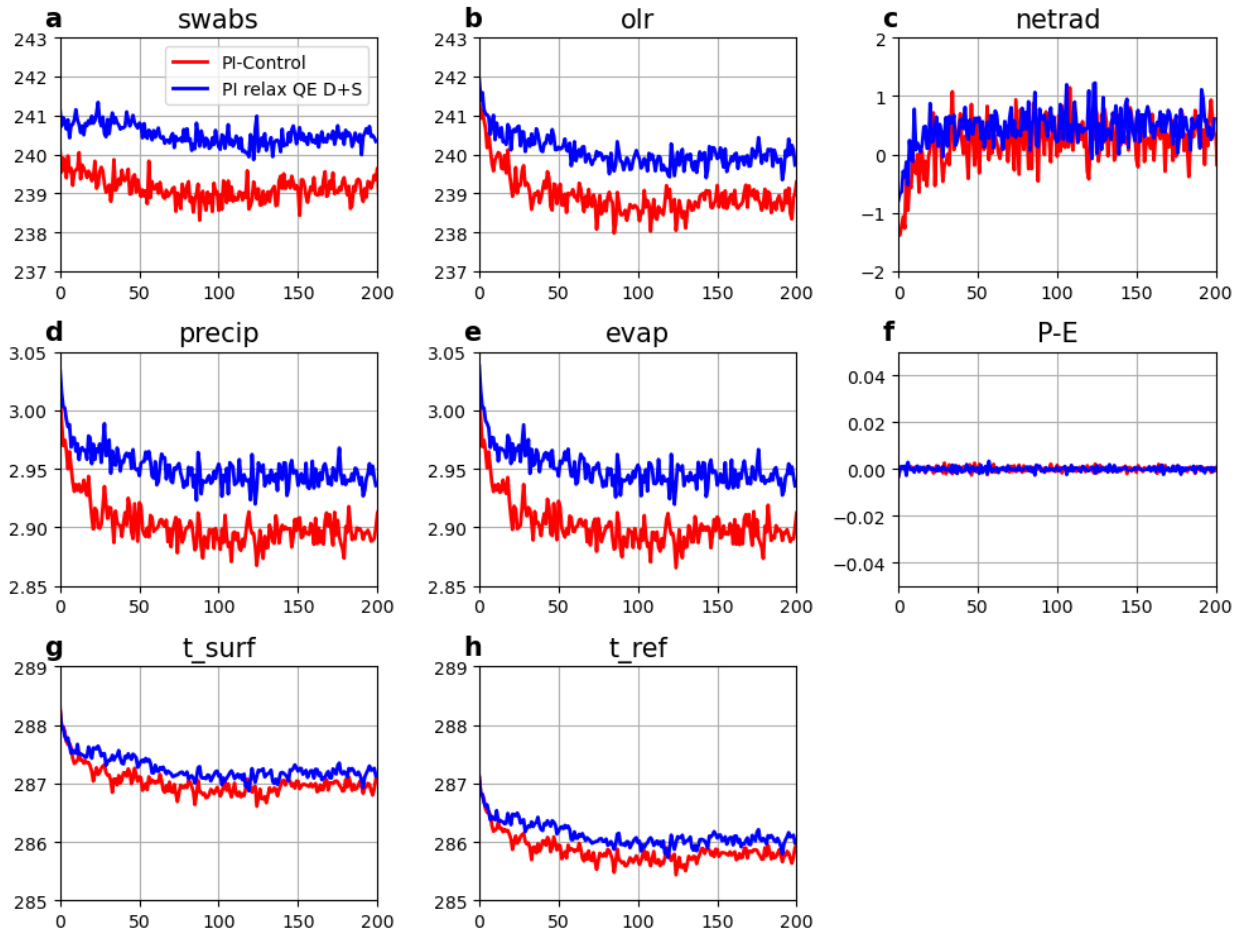


347
 348 Figure 12 Wave spectra from (a) standard AM4, (b) relax QE D+S and (c) IMERG.

349 3.3 Non-Equilibrium Convection in CM4

350 Model configurations that are apparently successful in uncoupled simulations do not
 351 always withstand coupling without deterioration of major simulation characteristics. In this
 352 section, we briefly compare results between PI-Control and PI relax QE D+S using CM4. PI-
 353 Control shows stable integrations with a reasonable TOA energy balance reported by Held et al.
 354 (2019). Noting that the 2001-2014 CERES-EBAF TOA SWABS is 241.0 W m^{-2} and OLR is
 355 240.2 W m^{-2} , PI relax QE D+S SWABS and OLR may be closer to their PI values than in PI-
 356 Control (Figure 13).

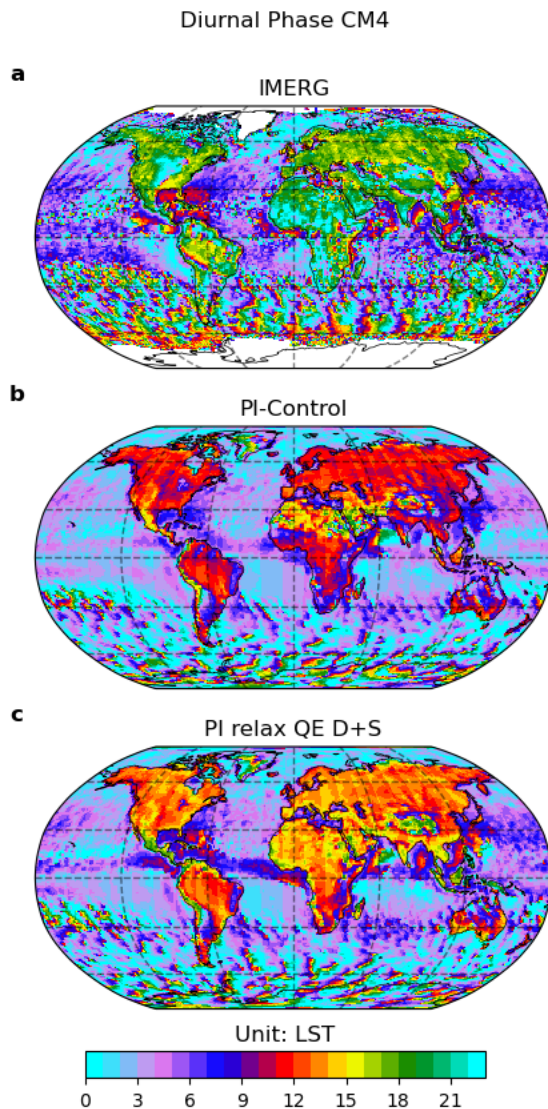
CM4



357

358 Figure 13 Global, annual-mean (a) SWABS (i.e. SW downward at TOA minus SW upward at
 359 TOA; W m^{-2}); (b) OLR (W m^{-2}), (c) net radiation (W m^{-2}), (d) precipitation (mm day^{-1}), (e)
 360 evaporation (mm day^{-1}), (f) precipitation minus evaporation (mm day^{-1}), (g) surface temperature
 361 (K), and (h) surface air temperature (i.e. temperature at 2m; K). Red solid lines are for PI-
 362 Control, while blue solid curves are for PI relax QE D+S.

363 Figure 14 shows that the improvements in the diurnal cycle of precipitation with relax QE
 364 D+S in AM4 are also evident in CM4. Biases in the diurnal precipitation cycle are reduced by
 365 several hours over most land areas, with improvements over many ocean regions as well.



366
 367 Figure 14 Same as Figure 2 but for the ocean-atmosphere coupled simulations using CM4.

368
 369 **4 Summary**

370 In this study, a new convective closure on the mass flux for deep convection is
 371 implemented in GFDL climate models AM4 (atmosphere-only simulations) and CM4 (ocean-
 372 atmosphere coupled simulations). The new convective closure is CAPE based and assumes a
 373 relaxed quasi-equilibrium between deep convection, shallow convection and non-convective
 374 processes (large-scale advection, surface fluxes, radiative transfer, eddy diffusion).

375 Over land, this new closure improves the diurnal cycle of precipitation with the diurnal
 376 phase biases reduced by half. The diurnal cycle of precipitation over ocean is also improved to

377 some extent. This indicates that shallow convection is key to delaying deep convection over land
 378 where boundary layer properties (to which shallow convection responds) change rapidly and
 379 plays a nonnegligible role in the presence of relatively slow-varying surface conditions like over
 380 some ocean regions.

381 Comparisons of the performance in AM4 and CM4 with the new convective closure
 382 against IMERG observations indicate that there is still room for improvement in simulating the
 383 diurnal cycle of precipitation during boreal summer. Future work may incorporate stochastic
 384 entrainment and effects from cold pools. One potential approach for parameterizing cold pools is
 385 to make the entrainment rate dependent on the mass flux from downdrafts and surface heat flux
 386 as illustrated in Suselj et al. (2019).

387

388 **Acknowledgments**

389 We thank Baoqiang Xiang and Wenhao Dong for their comments on the initial draft of
 390 this work.

391 **Data Availability Statement**

392 The standard AM4 and CM4 code can be found at
 393 <https://data1.gfdl.noaa.gov/nomads/forms/am4.0/> and <https://zenodo.org/records/3339397>. The
 394 code for non-equilibrium convection can be found at <https://zenodo.org/records/10709307>.
 395 IMERG datasets can be downloaded from
 396 [https://disc.gsfc.nasa.gov/datasets/GPM_3IMERGHH_07/summary?keywords=%22IMERG%20](https://disc.gsfc.nasa.gov/datasets/GPM_3IMERGHH_07/summary?keywords=%22IMERG%20final%20)
 397 [final%. GPCP data can be found at https://disc.gsfc.nasa.gov/datasets/GPCPMON_3.2/summary.](https://disc.gsfc.nasa.gov/datasets/GPCPMON_3.2/summary)
 398 CERES EBAF data can be found at <https://ceres.larc.nasa.gov/data/>. ERA5 data can be found at
 399 <https://cds.climate.copernicus.eu/cdsapp#!/dataset/reanalysis-era5-single-levels?tab=overview>.

400 **Appendix**

401 Donner and Phillips (2003) (their Figs. 1 and 2) show that CAPE is not in quasi-
 402 equilibrium at sub-diurnal time scales but instead changes following temperature and moisture
 403 changes in the planetary boundary layer:

$$404 \quad \frac{\partial \text{CAPE}}{\partial t} \cong (\partial_t \text{CAPE})_{\text{BL}} \leq \left(\frac{\partial \text{CAPE}}{\partial t} \right)_{\text{nc}} \quad (\text{A1})$$

405 $(\partial_t \text{CAPE})_{\text{BL}}$ is the total change in CAPE due to changes in PBL temperature and moisture
 406 by all physical processes, including convection. In (A1), the evolution of CAPE is controlled
 407 primarily by the PBL (Donner and Phillips (2003), their Fig. 1).

408 The failure of quasi-equilibrium,

$$409 \quad \frac{\partial \text{CAPE}}{\partial t} \ll \left(\frac{\partial \text{CAPE}}{\partial t} \right)_{\text{nc}} \quad (\text{A2})$$

410 to hold at sub-diurnal time scales has been compensated for by relaxing non-convective CAPE
 411 changes toward a threshold CAPE over a time of multiple hours, Eq. (3). Donner and Phillips
 412 (2003) (their Fig. 5) show that convective heat sources obtained by requiring convective
 413 tendencies to balance relaxed non-convective tendencies still agree rather poorly with convective
 414 heat sources diagnosed from observations. Accordingly, relaxed quasi-equilibrium for deep
 415 convection is augmented by a non-equilibrium term:

$$416 \quad \left(\frac{\partial \text{CAPE}}{\partial t} \right)_{\text{deep}} = - \frac{\text{CAPE} - \text{CAPE}_0}{\tau} + \left(\frac{\partial \text{CAPE}}{\partial t} \right)_{\text{non-equil}} \quad (\text{A3})$$

417 Analysis of non-convective tendencies of temperature and water vapor mixing ratio in
 418 Donner and Phillips (2003) (their Fig. 7) suggests:

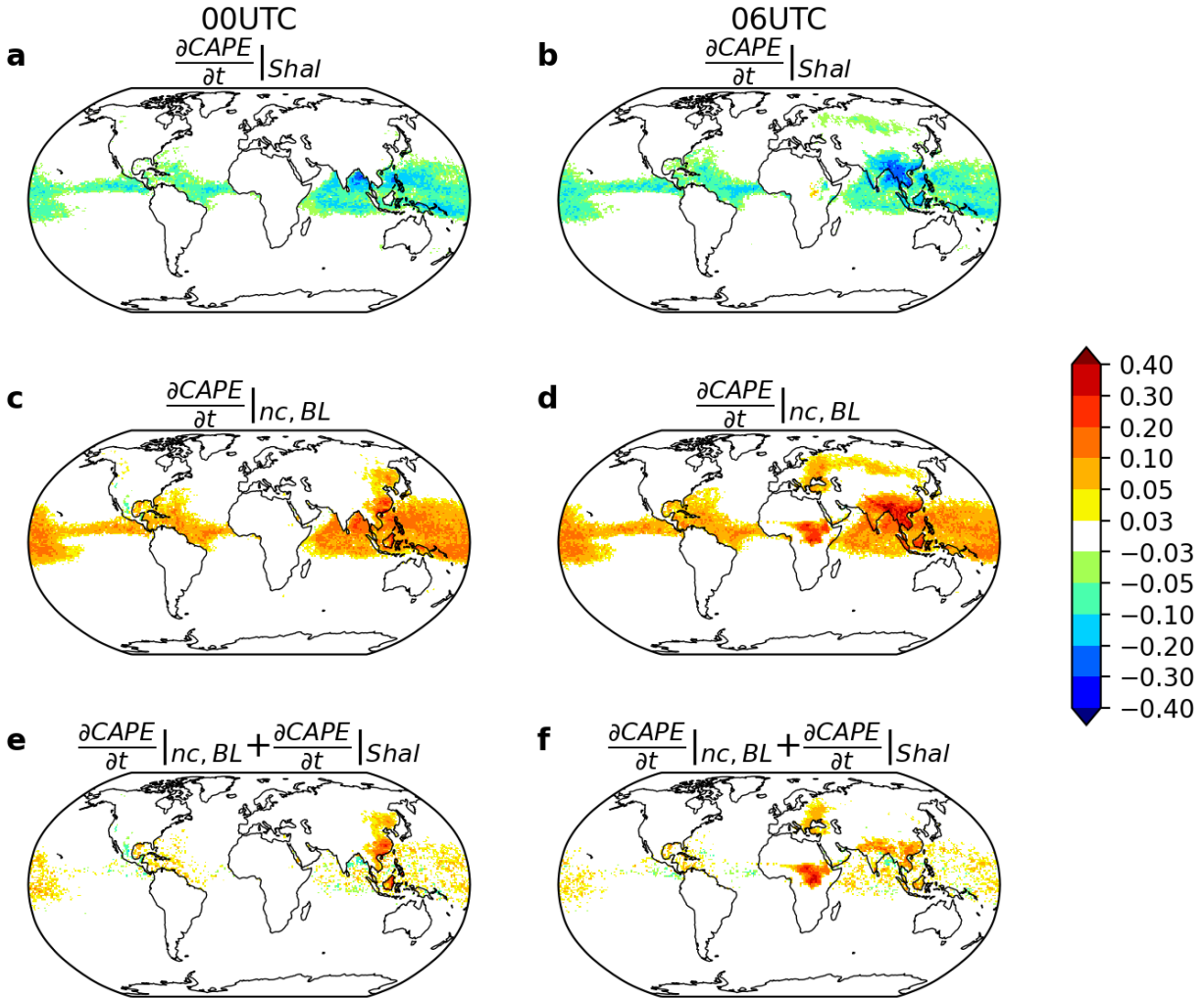
$$419 \quad \left(\frac{\partial \text{CAPE}}{\partial t} \right)_{\text{non-equil}} = \alpha \left(\frac{\partial \text{CAPE}}{\partial t} \right)_{\text{nc,BL}} \quad (\text{A4})$$

420 where α is a proportionality constant between 0 and 1, tending towards 1 with increasing non-
 421 convective PBL CAPE tendencies. (A4) is very similar to Eq. (14) in Bechtold et al. (2014).

422 Note that, for $\alpha = 1$, the non-equilibrium convective closures Eq. (4), (A3) and (A4) are
 423 identical if shallow CAPE tendencies are equal to the negative of the CAPE tendencies from
 424 non-convective PBL processes. Physically, this corresponds to shallow convection equilibrating
 425 non-convective PBL CAPE changes. In relax QE D+S, this holds to a limited degree. Figures A1
 426 and A2 show global patterns of instantaneous CAPE tendencies from shallow convection, non-
 427 convective PBL processes, and the sum of these tendencies composited four times daily. Non-
 428 convective CAPE tendencies are generally positive, driven by surface heat and moisture fluxes,
 429 which respond strongly over land to the diurnal cycle in surface shortwave absorbed radiation.
 430 Less frequently, this tendency can be negative and of smaller magnitude, for example, during
 431 nocturnal PBL cooling, e.g., Figure A1c over Mexico. CAPE tendencies from shallow

432 convection do not fully equilibrate non-convective PBL CAPE changes, and this is especially
 433 true over land when surface heating is most pronounced during the diurnal cycle (Figs. A1e,f and
 434 A2e,f).

435 A CAPE based non-equilibrium closure based on Eq. (A3) and (A4) with $\alpha = 1$ is
 436 referred to as D PBL CAPE Control. Figures A3a-c show the base mass fluxes from a relax QE
 437 D+S integration. The base mass fluxes are also calculated from a diagnostic call to D PBL CAPE
 438 Control closure in this integration. Figures A3d-f show the differences between the base mass
 439 fluxes diagnosed from the D PBL CAPE Control closure and those from relax QE D+S. In areas
 440 where relax QE D+S base mass fluxes are large and shallow CAPE tendencies do not equilibrate
 441 non-convective PBL CAPE tendencies in Figures A1 and A2, the diagnosed D PBL CAPE
 442 Control base mass fluxes are less in Figure A3. In regions with smaller relax QE D+S base mass
 443 fluxes, the D PBL CAPE Control mass fluxes can be larger. These regions do not support intense
 444 convection, and a wider range non-convective PBL CAPE tendencies likely occur. The sum
 445 $\left(\frac{\partial \text{CAPE}}{\partial t}\right)_{\text{shal}} + \left(\frac{\partial \text{CAPE}}{\partial t}\right)_{\text{nc,BL}}$ in these regions is often small (Figs. A1e,f and A2e,f).



446

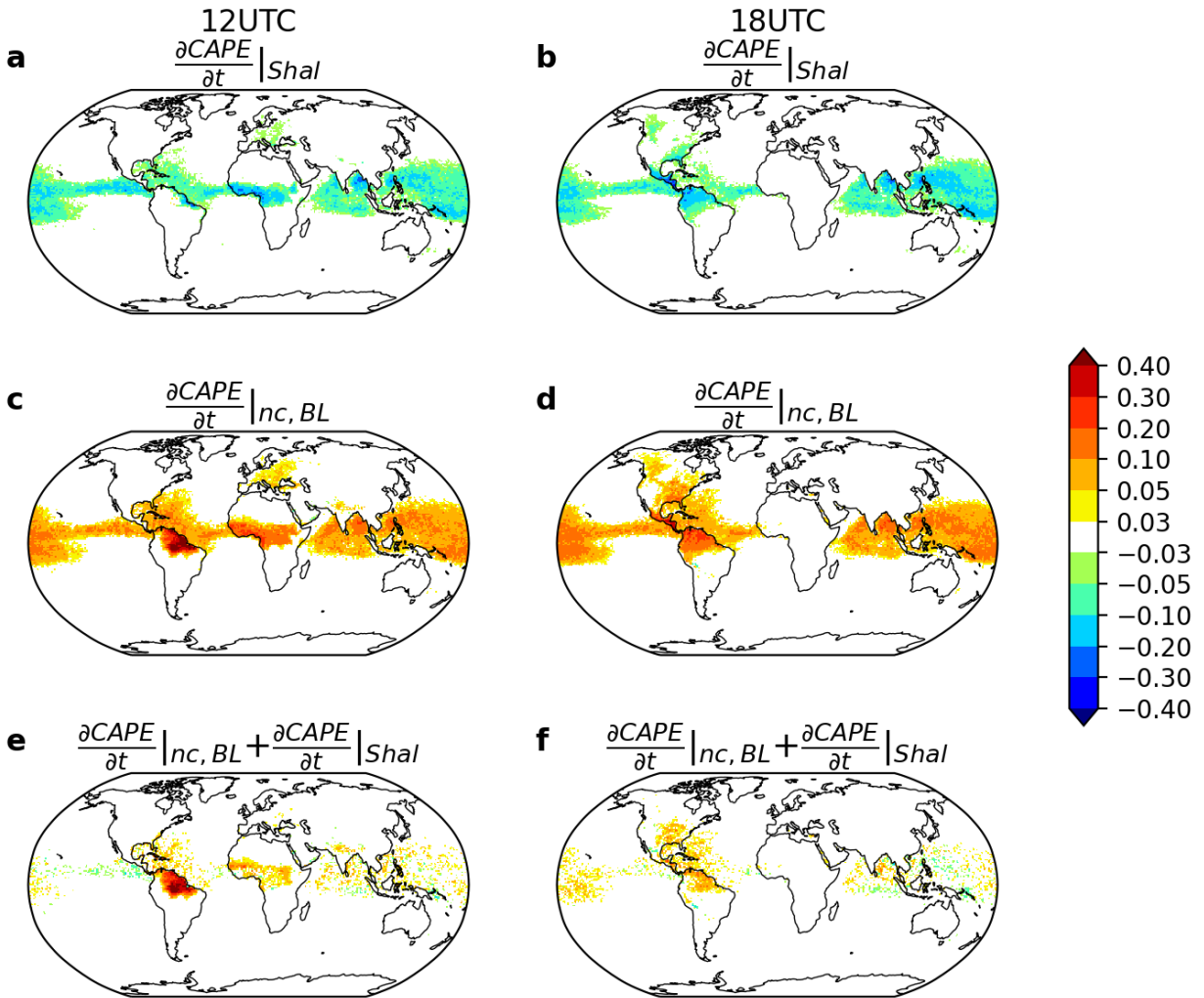
447

448

449

450

Figure A1 CAPE tendency due to shallow convection (panels a and b), CAPE tendency due to non-convective PBL processes (panels c and d), and the sum of them (panels e and f). The units for CAPE tendency are $\text{J kg}^{-1} \text{sec}^{-1}$. The left column is at 00 UTC and the right column is at 06 UTC.



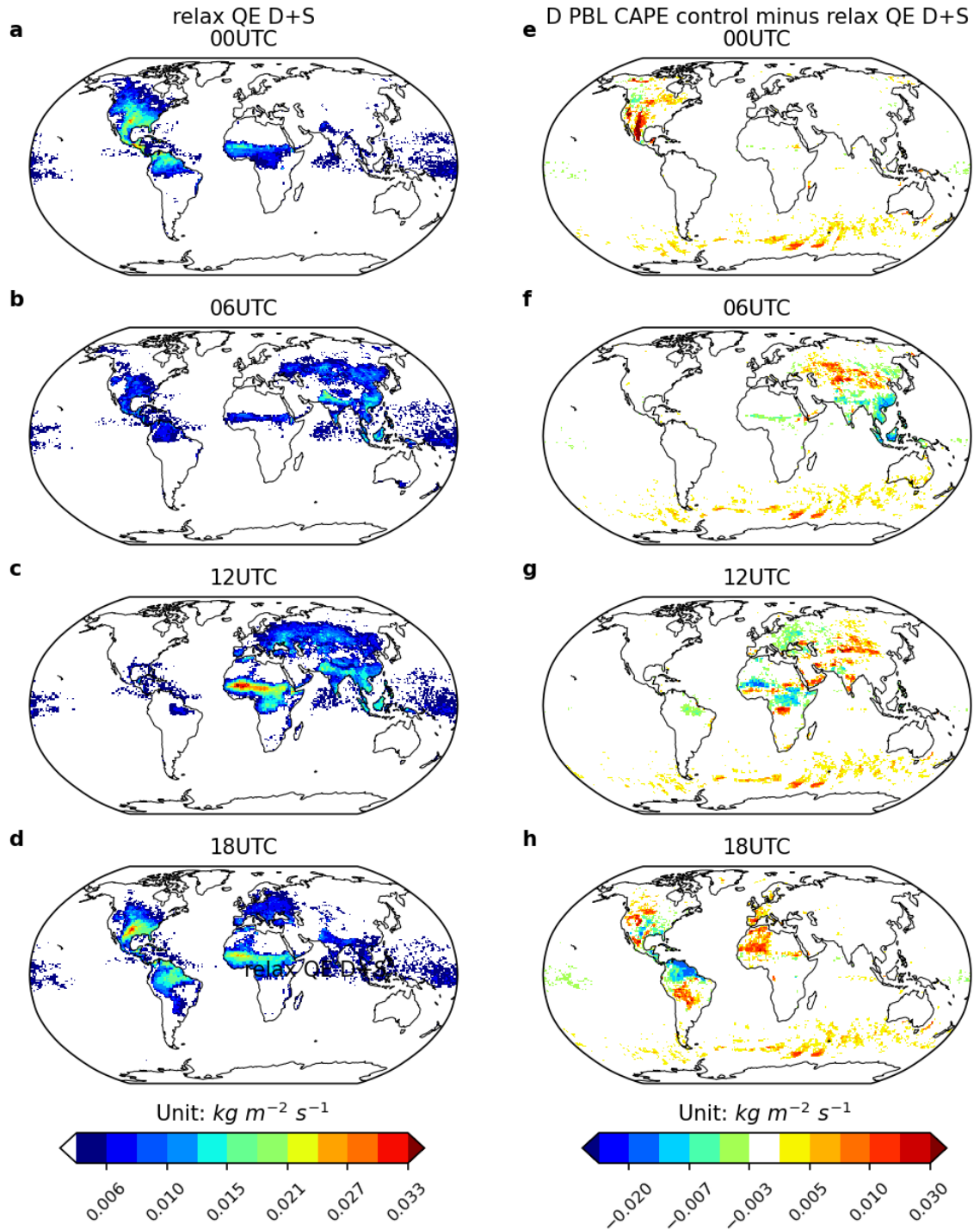
451

452

453

454

Figure A2 Same as Figure A1 but the left column is at 12 UTC and the right column is at 18 UTC. The units for CAPE tendency are $\text{J kg}^{-1} \text{sec}^{-1}$.



455

456 Figure A3 Cloud base mass flux computed from relax QE D+S (panels a-d), and the
 457 difference of cloud base mass flux between D PBL CAPE control and relax QE D+S (panels e-h)
 458 composited at 00, 06, 12 and 18 UTC. The units for cloud base mass flux are $\text{kg m}^{-2} \text{sec}^{-1}$.

459 **References**

- 460 Anderson, J. L., Balaji, V., Broccoli, A. J., Cooke, W. F., Delworth, T. L., Dixon, K. W., et al. (2004). The new
 461 GFDL global atmosphere and land model AM2–LM2: Evaluation with prescribed SST simulations.
 462 *Journal of Climate*, 17(24), 4641-4673.
- 463 Arakawa, A., & Schubert, W. H. (1974). Interaction of a cumulus cloud ensemble with the large-scale environment,
 464 Part I. *Journal of the atmospheric sciences*, 31(3), 674-701.
- 465 Bechtold, P., Köhler, M., Jung, T., Doblas-Reyes, F., Leutbecher, M., Rodwell, M. J., et al. (2008). Advances in
 466 simulating atmospheric variability with the ECMWF model: From synoptic to decadal time-scales.
 467 *Quarterly Journal of the Royal Meteorological Society: A journal of the atmospheric sciences, applied
 468 meteorology and physical oceanography*, 134(634), 1337-1351.
- 469 Bechtold, P., Semane, N., Lopez, P., Chaboureau, J.-P., Beljaars, A., & Bormann, N. (2014). Representing
 470 equilibrium and nonequilibrium convection in large-scale models. *Journal of the Atmospheric Sciences*,
 471 71(2), 734-753.
- 472 Bretherton, C. S., McCaa, J. R., & Grenier, H. (2004). A new parameterization for shallow cumulus convection and
 473 its application to marine subtropical cloud-topped boundary layers. Part I: Description and 1D results.
 474 *Monthly Weather Review*, 132(4), 864-882.
- 475 Cess, R. D., Potter, G., Blanchet, J., Boer, G., Del Genio, A., Deque, M., et al. (1990). Intercomparison and
 476 interpretation of climate feedback processes in 19 atmospheric general circulation models. *Journal of
 477 Geophysical Research: Atmospheres*, 95(D10), 16601-16615.
- 478 Dai, A., Giorgi, F., & Trenberth, K. E. (1999). Observed and model-simulated diurnal cycles of precipitation over
 479 the contiguous United States. *Journal of Geophysical Research: Atmospheres*, 104(D6), 6377-6402.
- 480 Davies, L., Plant, R., & Derbyshire, S. (2013). Departures from convective equilibrium with a rapidly varying
 481 surface forcing. *Quarterly Journal of the Royal Meteorological Society*, 139(676), 1731-1746.
- 482 Del Genio, A. D., & Wu, J. (2010). The role of entrainment in the diurnal cycle of continental convection. *Journal
 483 of Climate*, 23(10), 2722-2738.
- 484 Dong, W., Krasting, J. P., & Guo, H. (2023a). Analysis of Precipitation Diurnal Cycle and Variance in Multiple
 485 Observations, CMIP6 Models, and a Series of GFDL-AM4. 0 Simulations. *Journal of Climate*, 36(24),
 486 8637-8655.
- 487 Dong, W., Zhao, M., Ming, Y., Krasting, J. P., & Ramaswamy, V. (2023b). Simulation of United States mesoscale
 488 convective systems using GFDL's new high-resolution general circulation model. *Journal of Climate*,
 489 36(19), 6967-6990.
- 490 Donner, L. J., & Phillips, V. T. (2003). Boundary layer control on convective available potential energy:
 491 Implications for cumulus parameterization. *Journal of Geophysical Research: Atmospheres*, 108(D22).
- 492 Donner, L. J., Seman, C. J., Hemler, R. S., & Fan, S. (2001). A cumulus parameterization including mass fluxes,
 493 convective vertical velocities, and mesoscale effects: Thermodynamic and hydrological aspects in a general
 494 circulation model. *Journal of Climate*, 14(16), 3444-3463.
- 495 Donner, L. J., Wyman, B. L., Hemler, R. S., Horowitz, L. W., Ming, Y., Zhao, M., et al. (2011). The dynamical
 496 core, physical parameterizations, and basic simulation characteristics of the atmospheric component AM3
 497 of the GFDL global coupled model CM3. *Journal of Climate*, 24(13), 3484-3519.
- 498 Emanuel, K. A. (1991). A scheme for representing cumulus convection in large-scale models. *Journal of the
 499 atmospheric sciences*, 48(21), 2313-2329.
- 500 Fletcher, J. K., & Bretherton, C. S. (2010). Evaluating boundary layer–based mass flux closures using cloud-
 501 resolving model simulations of deep convection. *Journal of the atmospheric sciences*, 67(7), 2212-2225.
- 502 Fuchs, Ž., & Raymond, D. J. (2007). A simple, vertically resolved model of tropical disturbances with a humidity
 503 closure. *Tellus A: Dynamic Meteorology and Oceanography*, 59(3), 344-354.
- 504 Gerard, L., Piriou, J.-M., Brožková, R., Geleyn, J.-F., & Banciu, D. (2009). Cloud and precipitation
 505 parameterization in a meso-gamma-scale operational weather prediction model. *Monthly Weather Review*,
 506 137(11), 3960-3977.
- 507 Held, I., Guo, H., Adcroft, A., Dunne, J., Horowitz, L., Krasting, J., et al. (2019). Structure and performance of
 508 GFDL's CM4. 0 climate model. *Journal of Advances in Modeling Earth Systems*, 11(11), 3691-3727.
- 509 Hersbach, H., Bell, B., Berrisford, P., Hirahara, S., Horányi, A., Muñoz-Sabater, J., et al. (2020). The ERA5 global
 510 reanalysis. *Quarterly Journal of the Royal Meteorological Society*, 146(730), 1999-2049.
- 511 Hirons, L., Inness, P., Vitart, F., & Bechtold, P. (2013). Understanding advances in the simulation of intraseasonal
 512 variability in the ECMWF model. Part I: The representation of the MJO. *Quarterly Journal of the Royal
 513 Meteorological Society*, 139(675), 1417-1426.
- 514 Huffman, G., Behrangi, A., Bolvin, D., & Nelkin, E. (2022). GPCP Version 3.2 satellite-gauge (SG) combined
 515 precipitation data set, edited by Huffman. *GJ, Behrangi, A., Bolvin, DT, and Nelkin, EJ Greenbelt*,

- 516 *Maryland, USA, Goddard Earth Sciences Data and Information Services Center (GES DISC), <https://doi.org/10.5067/MEASURES/GPCP/DATA304> (last access: 12 August 2022).*
- 517
- 518 Huffman, G. J., Bolvin, D. T., Braithwaite, D., Hsu, K., Joyce, R., Xie, P., & Yoo, S.-H. (2015). NASA global
519 precipitation measurement (GPM) integrated multi-satellite retrievals for GPM (IMERG). *Algorithm*
520 *theoretical basis document, version, 4, 30.*
- 521 Jones, T. R., & Randall, D. A. (2011). Quantifying the limits of convective parameterizations. *Journal of*
522 *Geophysical Research: Atmospheres, 116*(D8).
- 523 Kain, J. S., & Fritsch, J. M. (1993). Convective parameterization for mesoscale models: The Kain-Fritsch scheme. In
524 *The representation of cumulus convection in numerical models* (pp. 165-170): Springer.
- 525 Kim, D., Sobel, A. H., Maloney, E. D., Frierson, D. M., & Kang, I.-S. (2011). A systematic relationship between
526 intraseasonal variability and mean state bias in AGCM simulations. *Journal of Climate, 24*(21), 5506-5520.
- 527 Lin, J.-L., Kiladis, G. N., Mapes, B. E., Weickmann, K. M., Sperber, K. R., Lin, W., et al. (2006). Tropical
528 intraseasonal variability in 14 IPCC AR4 climate models. Part I: Convective signals. *Journal of Climate,*
529 *19*(12), 2665-2690.
- 530 Loeb, N. G., Doelling, D. R., Wang, H., Su, W., Nguyen, C., Corbett, J. G., et al. (2018). Clouds and the earth's
531 radiative energy system (CERES) energy balanced and filled (EBAF) top-of-atmosphere (TOA) edition-4.0
532 data product. *Journal of Climate, 31*(2), 895-918.
- 533 Mapes, B. E. (2000). Convective inhibition, subgrid-scale triggering energy, and stratiform instability in a toy
534 tropical wave model. *Journal of the Atmospheric Sciences, 57*(10), 1515-1535.
- 535 Moorthi, S., & Suarez, M. J. (1992). Relaxed Arakawa-Schubert. A parameterization of moist convection for general
536 circulation models. *Monthly Weather Review, 120*(6), 978-1002.
- 537 Neelin, J. D., & Yu, J.-Y. (1994). Modes of tropical variability under convective adjustment and the Madden-Julian
538 oscillation. Part I: Analytical theory. *Journal of the atmospheric sciences, 51*(13), 1876-1894.
- 539 Pan, D. M., & Randall, D. D. (1998). A cumulus parameterization with a prognostic closure. *Quarterly Journal of*
540 *the Royal Meteorological Society, 124*(547), 949-981.
- 541 Petch, J., Brown, A., & Gray, M. (2002). The impact of horizontal resolution on the simulations of convective
542 development over land. *Quarterly Journal of the Royal Meteorological Society: A journal of the*
543 *atmospheric sciences, applied meteorology and physical oceanography, 128*(584), 2031-2044.
- 544 Piriou, J.-M., Redelsperger, J.-L., Geleyn, J.-F., Lafore, J.-P., & Guichard, F. (2007). An approach for convective
545 parameterization with memory: Separating microphysics and transport in grid-scale equations. *Journal of*
546 *the Atmospheric Sciences, 64*(11), 4127-4139.
- 547 Raymond, D. J., & Herman, M. J. (2011). Convective quasi-equilibrium reconsidered. *Journal of Advances in*
548 *Modeling Earth Systems, 3*(3).
- 549 Rayner, N., Parker, D. E., Horton, E., Folland, C. K., Alexander, L. V., Rowell, D., et al. (2003). Global analyses of
550 sea surface temperature, sea ice, and night marine air temperature since the late nineteenth century. *Journal*
551 *of Geophysical Research: Atmospheres, 108*(D14).
- 552 Rio, C., Hourdin, F., Grandpeix, J. Y., & Lafore, J. P. (2009). Shifting the diurnal cycle of parameterized deep
553 convection over land. *Geophysical Research Letters, 36*(7).
- 554 Stirling, A., & Stratton, R. (2012). Entrainment processes in the diurnal cycle of deep convection over land.
555 *Quarterly Journal of the Royal Meteorological Society, 138*(666), 1135-1149.
- 556 Stratton, R., & Stirling, A. (2012). Improving the diurnal cycle of convection in GCMs. *Quarterly Journal of the*
557 *Royal Meteorological Society, 138*(666), 1121-1134.
- 558 Suselj, K., Kurowski, M. J., & Teixeira, J. (2019). A unified eddy-diffusivity/mass-flux approach for modeling
559 atmospheric convection. *Journal of the Atmospheric Sciences, 76*(8), 2505-2537.
- 560 Tian, B., Held, I. M., Lau, N. C., & Soden, B. J. (2005). Diurnal cycle of summertime deep convection over North
561 America: A satellite perspective. *Journal of Geophysical Research: Atmospheres, 110*(D8).
- 562 Tiedtke, M. (1989). A comprehensive mass flux scheme for cumulus parameterization in large-scale models.
563 *Monthly Weather Review, 117*(8), 1779-1800.
- 564 Watters, D., Battaglia, A., & Allan, R. P. (2021). The diurnal cycle of precipitation according to multiple decades of
565 global satellite observations, three CMIP6 models, and the ECMWF reanalysis. *Journal of Climate, 34*(12),
566 5063-5080.
- 567 Xie, S., Wang, Y. C., Lin, W., Ma, H. Y., Tang, Q., Tang, S., et al. (2019). Improved diurnal cycle of precipitation
568 in E3SM with a revised convective triggering function. *Journal of Advances in Modeling Earth Systems,*
569 *11*(7), 2290-2310.
- 570 Yano, J. I., & Plant, R. (2012). Finite departure from convective quasi-equilibrium: Periodic cycle and discharge-
571 recharge mechanism. *Quarterly Journal of the Royal Meteorological Society, 138*(664), 626-637.

- 572 Zhang, G. J. (2002). Convective quasi-equilibrium in midlatitude continental environment and its effect on
573 convective parameterization. *Journal of Geophysical Research: Atmospheres*, 107(D14), ACL 12-11-ACL
574 12-16.
- 575 Zhang, G. J. (2003). Convective quasi-equilibrium in the tropical western Pacific: Comparison with midlatitude
576 continental environment. *Journal of Geophysical Research: Atmospheres*, 108(D19).
- 577 Zhang, G. J., & McFarlane, N. A. (1995). Sensitivity of climate simulations to the parameterization of cumulus
578 convection in the Canadian climate centre general circulation model. *Atmosphere-Ocean*, 33(3), 407-446.
579 <https://doi.org/10.1080/07055900.1995.9649539>
- 580 Zhao, M., Golaz, J. C., Held, I., Guo, H., Balaji, V., Benson, R., et al. (2018a). The GFDL global atmosphere and
581 land model AM4. 0/LM4. 0: 1. Simulation characteristics with prescribed SSTs. *Journal of Advances in*
582 *Modeling Earth Systems*, 10(3), 691-734.
- 583 Zhao, M., Golaz, J. C., Held, I., Guo, H., Balaji, V., Benson, R., et al. (2018b). The GFDL global atmosphere and
584 land model AM4. 0/LM4. 0: 2. Model description, sensitivity studies, and tuning strategies. *Journal of*
585 *Advances in Modeling Earth Systems*, 10(3), 735-769.
- 586